

Comparison of piece length and dynamics of large wood in streams covered with coniferous and broadleaf forests mapped using ortho-photographs acquired by an unmanned aerial vehicle

Haruka Tsunetaka (✉ tsunetakaharuka@ffpri.affrc.go.jp)

Forestry and Forest Products Research <https://orcid.org/0000-0001-7831-6193>

Slim Mtibaa

57880-Forestry and Forest Products Research Institute

Shiho Asano

57880-Forestry and Forest Products Research Institute

Takashi Okamoto

57880-Forestry and Forest Products Research Institute

Ushio Kurokawa

57880-Forestry and Forest Products Research Institute

Research article

Keywords: UAV, Large wood, Debris flow, Landslide

Posted Date: December 14th, 2020

DOI: <https://doi.org/10.21203/rs.3.rs-67734/v2>

License:  This work is licensed under a Creative Commons Attribution 4.0 International License.

[Read Full License](#)

Version of Record: A version of this preprint was published on March 26th, 2021. See the published version at <https://doi.org/10.1186/s40645-021-00419-6>.

Abstract

As large wood (LW) supplied by landslides and debris flows is one of the main components of watershed ecosystems, the importance of quantifying the dimensions of the LW is evident. However, the low accessibility of disturbed channels after landslides and debris flows generally impedes accurate and quick LW investigations. Recent advances in photogrammetry techniques may overcome such issues. In this study, we used ortho-photographs acquired using a small unmanned aerial vehicle (UAV) to measure the lengths of LW (wood pieces > 0.2-m long and > 0.03-m diameter) entrapped mainly by closed-type check-dams. We focused on two channels that are located in coniferous and broadleaf forests and affected by two different landslides events. The measurement accuracy was analyzed by comparing the lengths derived from the UAV method with direct measurements. When the both ends of a piece LW are satisfactorily extracted from an ortho-photograph acquired via the UAV, the LW lengths of coniferous trees can be measured with an accuracy of approximately ± 0.5 m. For broadleaf trees, most of the extracted lengths were shorter than the directly measured lengths, probably due to the low visibility arising from the complex structures of the root wad and the tree crown. Most LW pieces were discharged from landslide scars in the broadleaf forest, whereas approximately 750 LW pieces were left in the landslide scars of the coniferous forest. The number of LW pieces in the landslide scars increased with the increase in the landslide area, suggesting that some LW pieces can be left even if large landslides occur. There were no significant changes in the lengths or locations of the entrapped LW, at either site seven months after the first UAV flight. In the coniferous forests, the rainfall that triggered landslides in 2017 exceeded the 100-year return level, which was an abnormally intense rainfall. Although the 2019 rainfall event that occurred between UAV flights did not provide enough rainfall to trigger landslides, rainfall intensities with different durations reached the second-highest value from 1976 to 2019, exceeding the 30-year return period. This suggests that most of the entrapped LW rarely migrate even under extreme rainfall.

Introduction

Debris flow causes the entrainment of stand-woods located in initiation and riparian zones, and consequently it may include ~10%–60% of fluvial large wood (LW) by volume (Johnson et al., 2000; May and Gresswell, 2003a; Lancaster et al., 2003). In addition to its destructive impact on life and infrastructure (e.g., Ruiz-Villanueva et al., 2013), wood pieces in a debris flow can alter the flow regime because of their irregular shapes, which can be entrapped around obstacles and lead to anomalous deposition of sediment and inundations (e.g., May, 2002; Lancaster et al., 2003; Tang et al., 2018; Booth et al., 2020). The accumulation of LW results in structural peculiarities around channel networks (e.g., Keller and Swanson, 1979; Woodsmith and Buffington, 1996; Montgomery et al., 1996; Nakamura and Swanson, 2003). This contributes to changes in the ecosystem, the channel morphology, and the sediment flux through logjam formation and the decay of LW pieces (e.g., Wallace and Benke, 1984; Lisle, 1995; Montgomery et al., 1995; Gurnell et al., 2001; Comiti et al., 2006; Ruiz-Villanueva et al., 2016). Hence, the river form and function are determined by the interaction between water, sediment, and wood

(Nakamura et al., 2017; Swanson et al., 2020). Therefore, quantifying LW is important for assessing its impacts on ecological, geomorphological, and fluvial conditions.

Many previous studies focusing on LW pieces in streams have contributed to unraveling the role of LW in various spatiotemporal-scales and environmental settings, but most of these approaches required direct field measurements, such as local monitoring (e.g., Manners et al., 2007), the tracking of LW pieces (e.g., Ravazzolo et al., 2015; Wyzga et al., 2017), and field experiments using artificial wood pieces (e.g., Haga et al., 2002). Taking into account the diversity of forests around channels (e.g., age, species, and density of trees), the monitoring and field survey of LW pieces is evidently an effective approach. However, the necessity of human effort in the field hinders data acquisition in inaccessible areas (e.g., headwater channels and disturbed areas immediately after landslides and debris flows). In practice, field-data acquisition is difficult for a large-scale area exceeding the size of a sub-basin. The improvement of field-measurement techniques for LW thus remains a critical issue.

To address the measurement issues for LW, remote sensing approaches using three-dimensional data have been applied. The Use of LiDAR (light detection and ranging) data clearly reduces the processing time required for mapping logjams and LW (Kasprak et al., 2012; Abalharth et al., 2015; Atha and Dietrich, 2016). However, this technology is expensive and is therefore available only in some regions. Alternatively, photogrammetry based on structure-from-motion multi-view stereo (SfM-MVS) using a UAV (unmanned aerial vehicle) can produce three-dimensional data (e.g., digital-surface-models and point-clouds), which has been proven to be time-efficient compared to classical field surveys (Sanhueza et al., 2019). This approach overcomes data-availability issues and is relatively low cost. Nevertheless, most tests have been conducted in lowlands and flood plains rather than in low-accessibility areas such as steep channels (e.g., Sanhueza et al., 2019). As the accuracy of three-dimensional data acquired by SfM-MVS is greatly influenced by complex surfaces and obstacles—such as steep slopes, large reliefs, and vegetation coverage (e.g., Fonstad et al., 2013; James and Robson, 2014)—many unresolved uncertainties remain over the application of the SfM-MVS approach using three-dimensional data for LW measurements in steep and complex areas such as channels impacted by landslides and debris flows.

Aerial photography is a traditional source of two-dimensional data that may provide more-or-less meaningful information about LW. Even satellite images from Google Earth are being used for accurate LW mapping (Atha, 2013; Ulloa et al., 2015). Hence, the efficacy of aerial photography is evident, but the accuracy and effort of mapping depend on the image quality. In this respect, it is expected that small UAVs may allow the acquisition of high-resolution aerial photographs at low cost because of the lower flight altitudes and higher portability of UAVs compared to conventional aerial vehicles. Moreover, because flights of small UAVs can overcome inaccessibility issues and cover several kilometers, depending on the flight design, a UAV is a fairly attractive tool for obtaining LW measurements in low-accessibility areas.

In addition, LW is often quickly removed by river administrators to avoid unexpected damages in the downstream area resulting from its transport by streamflow after it is supplied to and entrapped in

streams (hereinafter this is referred to as secondary transport). The risk arising from the secondary transport of LW (e.g., damages on facilities in residential regions) has not been evaluated properly so far, because it has been difficult to conduct field surveys of the LW supply immediately after intense rainfall. In contrast, UAV flights can be conducted immediately after rainfall events that result in a large amount of LW, which can potentially contribute to unraveling LW dynamics after their supply and entrapment. Therefore, LW mapping can enable investigations of LW transport due to subsequent rainfall, even if it is carried out with a simple method using aerial photography. Nevertheless, the potential to measure LW based on aerial photographs acquired via UAV has not been thoroughly examined due to lack of sample cases.

In this study, we analyze the accuracy of UAV-based measurements for LW lengths. Two regions are selected representing two forest types, coniferous and broadleaf forests. In both regions, large amounts of LW were supplied to streams through landslides and debris flows triggered by a single rainfall event. This research has two main objectives: (1) to analyze the capability of ortho-photographs acquired via UAVs to measure the lengths of LW, and (2) to investigate whether entrapped LW pieces move again due to intense rainfall. Based on the results, we discuss the effectiveness of UAV measurements and how LW behave after their entrapment.

Study Sites

To examine the influence of tree type on the accuracy of LW measurements obtained using the ortho-photographs acquired by the UAV, we selected two different sites covered by coniferous or broadleaf forests (Figure 1a). Hereafter, the former site is referred to as the CF (coniferous forest) site (Figure 1b), while the latter site is referred to as the BF (broadleaf forest) site (Figure 1c). In this study, we use the term “tree type” to indicate either coniferous or broadleaf trees rather than the detailed tree species.

Coniferous forest site

The CF site is a sub-watershed of the Otoishi watershed located in the northern part of Kyusyu Island, Japan (Figure 1a, b). Its highest point is approximately 385 m above sea level (a.s.l.), and its lowest point is approximately 225 m a.s.l. The total length of the main channel is approximately 760 m with an average slope of approximately 12° (before the debris-flow occurrence), and the drainage area is approximately 0.15 km^2 . To prevent the destabilization of hillslopes and banks, five closed-type check-dams were constructed before the debris flow occurred in 2017 (Figure 2a). Most hillslopes are covered with artificial coniferous forests that consist mainly of *Cryptomeria japonica* and *Chamaecyparis obtusa*. The tree heights range from about 15 to 25 m.

In the region around the CF site, an intense rainfall on July 5, 2017, triggered more than 2,000 landslides, which resulted in debris-flow propagations and therefore a great amount of LW (Chigira et al., 2018). The sliding sediment layers were mainly granodiorite and pelitic schist (Chigira et al., 2018). The intense rainfall in July 2017 triggered six landslides at the CF site (Figure 2a), but the existing check-dams

effectively prevented the descent of sediment and LW. Hence, most of the LW pieces were trapped around the check-dams and along the channel, thereby preventing damage in the downstream residential areas. Because of this low impact on the residences, the LW pieces were not removed and were left *in-situ* until the time we carried out observations.

Broadleaf forest site

The BF site is located in the Hiroshima prefecture in the western part of Japan (Figure 1c). Here, two channels are confluent at an irrigation pond that is located at the lower ends of channels (~305 m a.s.l., Figure 2b). The highest points of channels A and B are ~410 and ~480 m a.s.l., respectively. Their total lengths are ~880 and ~466 m, respectively. The average slopes of the two channels are similar, at ~11°–12° (before the debris-flow occurrence). The drainage areas of channels A and B are ~0.07 and ~0.13 km², respectively. Similar to the case of the CF site, four closed-type check-dams were constructed before the debris flow occurred in 2018 (Figure 2b). The forest type is completely different, and most of the hillslopes are covered by broadleaf forests with various tree types. The tree heights range from about 10 to 20 m.

In the Hiroshima prefecture, a stationary front affected by Typhoon Prapiroon caused heavy rainfall on July 5–7, 2018 (Tsuguti et al., 2019) and triggered approximately 8,000 landslides due to the vulnerable geological setting, which is mainly dominated by weathered granite (Kaibori et al., 2018). Five landslides occurred at the BF site, but the check-dams and the pond effectively prevented the descent of sediment and LW. Similar to the situation at the CF site after the disaster, the LW pieces produced in the BF site were left *in-situ* until we carried out the observations.

Methods

This study consists of two parts: (1) an assessment of the accuracy of the LW measurements obtained from ortho-photography acquired via the UAV, and (2) rainfall analysis to investigate the possible transport of entrapped LW.

UAV flights and aerial-photograph processing

A small consumer-grade UAV (DJI Mavic 2 pro; Table 1) was used for the flights covering the channels and landslides (Figure 2). Two UAV flights were conducted at each of the respective study sites (Table 2): (1) February 14 and September 26, 2019, at the CF site, and (2) November 16, 2018, and December 25, 2019, at the BF site. The flights were conducted manually at elevations between about 50 m and 200 m, and most of the photographs were taken in the nadir direction. The flight path provided at least a 70% overlap in the aerial-photographs. To reduce differences in shade and brightness among the acquired aerial-photographs, the flights were operated to avoid strong sunlight.

The acquired images were processed using SfM-MVS photogrammetry software (Agisoft, Metashape Professional version 1.5.1). Usually, artificial reference markers are established, and their absolute coordinates are measured using the GNSS (global navigation satellite system) to provide ground-control points (GCPs) for geo-referencing of the SfM-MVS photogrammetry (e.g., Barnhart et al., 2019; Tsunetaka et al., 2020). Unlike this approach, in most cases, immediately after a debris-flow disaster, LW pieces generally impede the establishment of artificial reference markers as LW pieces behave as obstacles. The recently developed, high-accuracy, RTK (real time kinematic) GNSS-based direct geo-referencing system built into SfM-MVS photogrammetry processing makes it possible to obtain accurate absolute coordinates without GCPs (e.g., Carbonneau and Dietrich, 2017). However, the consumer-grade UAV we used does not include such an RTK-GNSS system, because it is an expensive technology. Because of these operational limitations, we focused on the ability to make LW measurements using relatively low-cost UAV-based processing. Our intention was thus to assess the accuracy of measurements using only UAV flights without any other field operations (e.g., setting artificial reference-markers) or RTK-GNSS systems.

The position data from the built-in GNSS used for controlling the flight position is contained in exchangeable image file format data for each photograph, and we used it to make preliminary corrections to the coordinates of the processed ortho-photographs. Following standard SfM-MVS photogrammetry workflow, the ortho-photographs were produced with a spatial resolution of 0.03–0.05 m. Because the measurements were performed without establishing artificial reference markers, the coordinates of the resulting ortho-photographs taken during the different flight dates did not overlap accurately. As the principal aim of using sequential ortho-photographs was to investigate the transport of the LW, it is necessary only to have relative coordinate system overlap (i.e., absolute coordinate system overlap is not required). Thus, we manually adjusted two sequential ortho-photographs by using the crests of the check-dams as GCPs for which the coordinates were taken from the older ortho-photograph. Using the extracted coordinates, the ortho-photograph acquired on the later date was transformed to fit the first one. The differences in the lengths of selected immobilized objects (e.g., large boulders and the crests of check-dams) were less than approximately 0.2 m. Therefore, we consider the horizontal accuracy of the ortho-photographs to be less than 0.2 m.

Accuracy assessment

Because we used ortho-photographs (i.e., two-dimensional data) to quantify the LW, the dimension of LW measured by the UAV is its length. First, we extracted the length of the LW, both as a single piece and as an element of a jam-forming log as line data from the acquired ortho-photographs. Note that invisible LW pieces below a jam-forming log are out of the measurement target. All visible LW pieces were extracted at the CF site (the area surrounded by the dotted white line in Figure 2a), whereas only LW pieces around the check-dams A and B were investigated at the BF site because of the low visibility of LW originating from broadleaf trees (Figure 2b). Accordingly, the measurement range differed from a reach scale at the BF site to a sub-watershed scale at the CF site.

The measurement accuracy of the extracted length is presumably affected by visibility, which is related to the types and sizes of the trees. Moreover, because LW is often inclined and broadleaf trees have a curved shape, orthogonal projection to obtain the extracted length may cause a measurement error (Figure 3). Hence, we focused on the differences due to tree types (i.e., either coniferous or broadleaf trees), diameter, and entrapment inclination of the LW.

To compare with the extracted lengths of the LW, we directly measured LW pieces at the study sites (Figure 3). Based on the ortho-photographs from the first flight, the visible LW pieces were labeled. When we conducted the second flight, we found and directly measured some of the labeled LW pieces (50 LW pieces at the CF site and 131 LW pieces at the BF site). In the found LW pieces, we measured the lengths—excluding the root-wads and twigs—directly using a tape (estimated precision <5 cm), similar to the approach of Sanhueza et al. (2019) and compared those measurements with the lengths extracted from the ortho-photographs from the first UAV flight (Figure 3). Using the same tape, we measured the circumferences of the found LW pieces at approximately 1.0 to 1.5 m height from the root-wad. For LW pieces less than approximately 1.5 m in length, because there were only slight differences in the thickness of a single fragment, we measured the circumference at an arbitrary location. From the measured circumferences, we calculated the diameter of each found LW piece. At the CF site, as the LW retained relatively straight shapes, the entrapment inclination was measured directly using an angle meter (estimated precision < $\pm 1^\circ$, Figure 3a).

The extraction of LW depends on its visibility in the ortho-photographs, and thus the identification of its origin as well as the detection of small wood pieces of less than the minimum resolution of the ortho-photographs (i.e., 0.03 m in diameter) would go beyond the measurement purpose. Although LW is typically defined as a wood piece > 0.1 m in diameter and > 1 m in length (e.g., Jackson and Sturm, 2002; Tang et al., 2018), we defined LW as wood pieces > 0.03 m in diameter and > 0.2 m in length in this study, following the minimum measured diameters and lengths of the LW. Moreover, the extracted LW may contain multiple pieces that originated from a single tree. Note that, as a single stand-wood may result in several pieces of LW, counting the extracted LW involves uncertainty.

Analysis to determine the transport of large wood

To analyze whether or not LW migrated through time, we created the quantile–quantile (Q–Q) plots of the probability density of the extracted length. The CF site was divided into seven zones: six landslide scars and the riparian zone with a channel approximately 760 m in length (Figure 2a). Changes in the probability density of the LW length were visually tested using the Q–Q plots. Similarly, Q–Q plots were made for channels A and B at the BF site (Figure 2b). For each zone, to investigate the coincidence of the probability density of the extracted length between the two flight dates (Table 2)—(1) February and September, 2019 (i.e., approximately seven months), at the CF site, and (2) November, 2018, and December, 2019 (i.e., approximately eleven months), at the BF site—we conducted a goodness-of-fit test using the Kolmogorov–Smirnov test.

In addition, we investigated whether specific rainfall characteristics triggered the secondary transport of LW. For this reason, we used the hourly rainfall records from 1976 to 2019 obtained at the closest rain-gauges installed by the Japan Meteorological Agency, the Asakura station (for the CF site, Figure 1b) and the Higashihiroshima station (for the BF site, Figure 1c). The annual maxima of rainfall intensity of various durations (1, 2, 3, 6, 12, 24, 48, and 72 hours) were investigated from 1976 to 2019 and compared with the intensity of the rainfall that triggered the debris flows. In addition, we examined the records of rainfall maxima after the debris-flow occurrence. The return periods were calculated based on the probability density of each rainfall intensity fitted by a Gumbel distribution based on the annual maxima (e.g., Koutsoyiannis et al., 1998; Sane et al., 2018). For this fitting process, the goodness-of-fit test (Kolmogorov–Smirnov test) resulted in p -values exceeding 0.1, suggesting that the applied Gumbel-distribution models fitted the probability density of the observed rainfall well.

Results

Lengths of the entrapped large wood

As expected, the comparison of the extracted and measured lengths of the LW indicates that the measurement accuracy depends on the visibility of the LW. Fifty pieces of LW were directly measured at the CF site (Figure 4a). Fourteen of them were trapped by stand-woods located in the riparian zone, and they were partially invisible from the sky due to the coverage by the tree crowns. This low visibility caused underestimates of the extracted lengths, with errors in length being a maximum at ~10 m. In contrast, 36 other pieces were fully visible, and their lengths ranged between about 3 m and 22 m. Despite this wide range, most measurements coincided well with the extracted lengths. This clear dependence on the visibility of the LW is reflected in the boxplot (Figure 5), indicating that the interquartile ranges obviously differed between the visible and covered LW; the differences ranged from -0.4 to 0.5 m and from 1.6 to 4.3 m, respectively (Figure 5).

The lengths of 130 LW pieces without crown coverage were directly measured at the BF site, but they rarely coincided with the extracted lengths, which were usually underestimates (Figure 4b). Moreover, the differences between the lengths varied. The related interquartile range varied between approximately 0.3 m and 2.1 m, reflecting the low accuracy and high uncertainty in the measurement of broadleaf trees compared to coniferous trees (Figure 5).

Strictly speaking, the extracted length was the orthogonally projected length, and we therefore calculated the slope distance of the measured LW from the extracted length using the measured slope. However, this correction did not significantly improve the measurement accuracy because differences in the visibility of the LW depending on the difference in the tree types overwhelmed the influence arising from the approximation by the orthogonal projection (Figures 4a and 6). The differences in the diameters of the LW indicate that the extracted lengths of relatively narrow pieces (<~0.2–0.3 m in diameter) at the BF site tend to be underestimated (Figure 7), despite the absence of crown and logjam coverages. This suggests

that the decrease in the visibility of small-diameter pieces was responsible for the decrease in measurement accuracy at the BF site.

Most LW pieces were discharged from landslide scars at the BF site, whereas a total of approximately 750 LW pieces (exceeding 50% of the total of ~1,370 LW pieces) were left in the landslide scars at the CF site. At the CF site, the interquartile of the length of the LW differed slightly among the landslide scars, but they were similar between the riparian zone and the average of all landslides: 2.5 to 7.7 m and 2.6 to 8.3 m, respectively (Figure 8a). The median length of the LW ranged from 3.4 m (in landslide 4) to 7.8 m (in landslide 1). At the BF site, the interquartile of the length of the LW at check-dams A and B were 1.1 to 3.1 m and 0.8 to 2.6 m, respectively (Figure 8b). The median lengths of the LW at check-dams A and B were similar: 1.8 m and 1.5 m, respectively. The median length of the LW at the CF site was ~4.5 m, which is evidently greater than that at the BF site (Figure 8c).

The areas of the landslide scars at the CF site ranged widely, from ~800 to 5,400 m² (Figure 9). The number of entrapped LW pieces tended to increase with the increase in the area of the landslide scars (Figure 9). Landslide 2 (~5,400 m²) accounted for approximately 40% of the total area of the landslide scars (i.e., the total landslide area at the CF site is ~14,000 m²), and thus this landslide was the predominant sediment source at the CF site. Despite this huge sediment discharge, the number of entrapped LW pieces was highest among the landslide scars, at approximately 350 LW pieces.

Transport of entrapped large wood

At both sites, there were only slight visible changes in the spatial distribution of the LW between the two ortho-photographs (Figures 10 and 11). The LW pieces were trapped in various areas—for instance, as stand-woods in the riparian zone, the check-dams, and the landslide areas. Despite these differences in the entrapment zones, it seems that most of the LW did not move even after about 7 months (at the CF site, Figure 10) and over one year (at the BF site, Figure 11). The Q–Q plots indicate that the probability density of the extracted LW length coincided well with the measured length, regardless of the division of the entrapment zones (Figure 12). Thus, the *p*-values with respect to the goodness-of-fit test exceeded 0.05, suggesting that the changes were statistically nonsignificant.

The rainfall anomalies that triggered debris flows were revealed by comparing the annual maxima of the rainfall intensity in each case. At the CF site, the rainfall that triggered the debris flow in 2017 was obviously excessive rainfall, as the rainfall intensity was the highest compared with the annual maxima of other years, regardless of the rainfall duration (Figure 13a). This suggests that the highly intense and continuous rainfall resulted in the large amount of LW. At the BF site, for the rainfall that triggered debris flows in 2018, rainfall intensities with 1–6 hour durations were not higher than the other annual maxima since 1976, but those with 12–72 hour durations were the most intense since 1976 (Figure 13b). This suggests that a high rainfall intensity continuing over 12 hours resulted in landslides and debris flow accompanied by the propagation of LW. Both rainfall events that triggered debris flows at the CF and BF sites reached levels exceeding the 100-year return period (Tables 3 and 4).

At the BF site, after the landslides and debris flows in 2018, the maximum annual rainfall intensity in 2019 was not remarkable (Figure 13b, Table 4). Thus, although most LW pieces remained in place, it is difficult to analyze the potential of secondary transport of entrapped LW via intense rainfall. In contrast, at the CF site, after the landslides and debris flows in 2017, the annual rainfall intensity maxima in 2018 and 2019 were the second or third highest values since 1976 (Figure 13a). Although the intensity of the triggering rainfall in 2017 significantly exceeded the annual maxima in 2018 and 2019 in terms of the return period, some rainfall intensities in 2018 and 2019 exceeded the level of the 30-year return period (Table 3). Such a heavy rainfall event occurred on July 21, 2019 (in between the UAV flights at the CF site; Table 2).

Discussion

Implications for UAV-based large wood mapping

Our results demonstrate that the visibility and tree types of the LW determine the ability to measure their lengths accurately using ortho-photographs acquired via UAVs. The lengths of most of the LW pieces originating from coniferous trees were measured with better than ± 0.5 m accuracy using the ortho-photographs acquired by the UAV, but for the broadleaf trees, the lengths were underestimated systematically despite the absence of tree-crown coverage reducing the visibility (Figures 4b and 5). Considering the complex structures of both ends of the broadleaf trees (i.e., wide and rounded crowns and root-wads; Figure 3b), these underestimates may be attributed to missing extractions due to the low visibility of the broadleaf trees arising from the complex structures at the ends. In addition, the lengths of the entrapped LW at the BF site was less than that at the CF site (Figure 8), implying the fragmentation of broadleaf trees during the debris flow. Although the characteristics of the debris flow also probably influence the magnitude of LW fragmentation (e.g., Johnson et al., 2000; Lancaster et al., 2003), the fragility of broadleaf trees may reduce the measurement accuracy based on the ortho-photograph at the BF site by decreasing the visibility of the LW.

Hence, most of the factors that decrease the measurement accuracy of LW depend on visibility. Based on this interpretation, LW measurements via UAV have both positive and negative aspects. Several components that affect the quality of the aerial photographs (e.g., black shadows, brightness involving overexposure, and overlap ratios among the aerial photographs) depend on the weather conditions and the flight plan (e.g., the path, height, and direction of shooting). For example, it is expected that low flight altitudes and flights under cloudy conditions can avoid block-out shadows and blown-out highlights in the acquired UAV images, resulting in an increase in the visibility of LW in the processed ortho-photographs. Thus, an adequate flight plan may significantly improve the accuracy of UAV-based LW measurements, without additional processing in the SfM-MVS photogrammetry.

Conversely, our results reveal an obvious limitation of ortho-photograph-based measurements. In general, LW is not only dispersed along a channel, but also results in logjam due to stacking and accumulation (e.g., Manners et al., 2007; Abalharth et al., 2015). However, the correlation between measurement

accuracy and visibility from the sky demonstrates that the length measurements of LW pieces covered by a logjam are beyond the scope of ortho-photograph-based measurements. Sanhueza et al (2019) pointed out that vegetation in streams also may cover LW pieces and thus decrease the measurement accuracy of LW pieces based on images acquired by UAV. Indeed, the tree-crown coverage decreased the measurement accuracy of LW length (Figure 4a). Given these measurement limitations, it is especially difficult to measure jam-forming LW pieces in streams deeply covered by vegetation (e.g., riparian trees) using the approach employing images acquired by a UAV.

In other words, the total amount of LW is probably underestimated in all UAV-based measurements. In this respect, the entrapment of LW pieces in landslide scars at the CF site may also have been underestimated, suggesting that high-ratio LW pieces were left even in slipped hillslopes. In some sub-watersheds with coniferous forests located around the CF site, no LW pieces were left in the landslide scars (Marutani et al., 2017). Thus, the difference in tree type (i.e., coniferous or broadleaf trees) cannot account for the high-ratio of LW entrapments in the landslide scars at the CF site compared with that at the BF site. The median length of LW varied among landslide scars (Figure 8a), probably depending on differences in runout processes and sediment volume among landslides. Considering this, the increase in the number of entrapped LW pieces with the increase in the landslide area (Figure 9) indicates that LW pieces may remain in landslide scars regardless of differences in size and the dynamics of landslides. It seems that the outlets of landslide scars at the CF site are relatively narrow (like bottle-necked shapes) compared with those at the BF site (Figure 2), which may lead to high-ratio LW entrapments.

Possibility of the transport of the entrapped large wood

The slight changes in the lengths and spatial distributions of the LW suggest that the LW pieces that were entrapped by the check-dams did not move after the debris-flow disaster (Figures 10, 11, and 12). The elapsed time from the first flight was about seven months for the CF site and over a year for the BF site (Table 2), which may be insufficient to cause significant visible decay. This means that intact LW still remains in the upper reaches of the channels. However, considering the slight differences in the spatial distribution and the Q–Q plot of the LW at the CF site (Figures 10 and 12), the extremely high rainfall intensities in 2019 (Figure 13a and Table 3) suggest that most of the entrapped LW remains in place and rarely migrates, even when intense rainfall exceeding the level of the 30-year return period occurs. This implies that most rainfall events that do not cause debris flows and landslides cannot trigger secondary transport of entrapped LW.

Because the pre-existing check-dams trapped LW at both sites, differences in the trend between such artificial trapping and natural entrapment of LW should be noted. Even so, the low transportability of the entrapped LW provides insight into the role of the LW and sediment deposited in the upstream channel after debris flows and landslides. The efficacy of LW trapping by closed-type check-dams is generally considered relatively low compared with that of open-type check-dams (e.g., Piton and Recking, 2016).

Nevertheless, the entrapment of LW pieces by closed-type check-dams continued in the long term, due to the low possibility of secondary transport at our study sites. May and Gresswell (2003b) argued that LW pieces in streams can facilitate sediment deposition, thereby resulting in an increase in sediment storage. Indeed, the low transportability of the entrapped LW pieces in the CF and BF sites indirectly indicates low erosion and discharge rates of the sediment stored after a landslide occurrence, suggesting that the entrapped LW pieces can impede subsequent sediment transport. For this reason, the trapping of LW pieces in low-order streams during and immediately after a landslide occurrence is notably important in mitigating subsequent impacts on facilities in residential regions due to the LW pieces and sediment supplied.

Conclusions

We mapped large wood (LW) pieces using ortho-photographs acquired using a UAV in two headwater channels covered by coniferous or broadleaf forests (the CF and BF sites, respectively) to: (1) determine whether or not ortho-photography acquired via UAV allows measurements of the lengths of the LW, and (2) to investigate the possibility of the transport of entrapped LW by intense rainfall.

At the CF site, comparing the directly measured lengths with the lengths extracted by UAV mapping indicates that aerial-photography measurements had approximately ± 0.5 m accuracy when the both ends of the LW were satisfactorily visible. In contrast, some LW pieces were trapped by stand-woods in the riparian zone, which were invisible underneath the tree crowns, and this led to underestimation of the extracted lengths. At the BF site, most of the extracted length values were shorter than the lengths measured directly, probably due to low visibility of the ends of the LW pieces due to complex tree structures in the root-wads and tree crowns. Hence, these results suggest that the measurement accuracy of LW via UAV strongly depends on the visibility of the LW arising from tree types. In other words, although flight operations that adequately increase the visibility of LW in UAV images may improve the accuracy of LW length measurements, the UAV-image-based approach is fundamentally inadequate for measuring jam-forming LW pieces, especially in streams covered by riparian trees.

Most LW pieces did not remain in the landslide scars at the BF site, whereas approximately 750 LW pieces were left in the landslide scars at the CF site. The number of LW pieces in the landslide scar tended to increase, depending on the increase in the landslide area. Therefore, even large landslides cannot transport all LW pieces from their slip hillslopes in some cases, suggesting that LW pieces may remain in landslide scars regardless of the landslide area.

At both sites, changes in the frequency distribution of the lengths and the locations with respect to entrapped LW were slight even over seven months had passed since the first mapping. Nevertheless, at the CF site, some rainfall intensities between the two flights reached the second-highest values since 1976. Although the rainfall intensity that triggered the landslides in 2017 was higher than the annual maxima in 2019, some intensity values in 2019 exceeded the 30-year return period. This suggests that most of the entrapped LW remains and rarely migrates again, even under intense rainfall.

Abbreviations

BF: Broadleaf forest; CF: Coniferous forest; GCP: Ground-control point; GNSS: Global navigation satellite system; LW: Large wood; LiDAR: Light detection and ranging; SfM-MVS: Structure-from-motion multi-view stereo; UAV: Unmanned aerial vehicle

Declarations

Availability of data and material

The data used in this paper are available from the authors upon request.

Competing interests

The authors declare that they have no competing interest.

Funding

This work was supported by the project “Development of technology for impacts, mitigation and adaptation to climate change in the sectors of agriculture, forestry and fisheries” of the Agriculture, Forestry and Fisheries Research Council.

Authors' contributions

HT conducted field measurements using a UAV and data analysis, and drafted this manuscript. SM conducted field measurements and rainfall processing. SA, TO, and UK carried out field measurements. All authors read and approved the final manuscript.

Acknowledgements

The authors are grateful to the staffs of Forest Agency, Japan, for their assistance in the field observations. The constructive anonymous reviews significantly improved the quality of the paper and are greatly acknowledged.

References

Abalharth M, Hassan M, Klinkenberg B, Leung V, McCleary R (2015) Using LiDAR to characterize logjams in lowland rivers. *Geomorphology* 246:531-541

Atha JB (2013) Identification of fluvial wood using Google Earth. *River Research and Applications* 30(7):857-864

Atha JB, Dietrich JT (2016) Detecting fluvial wood in forested watersheds using LiDAR data: a methodological assessment. *River Research and Applications* 32(7):1587-1596

- Barnhart KR, Rengers FK, Ghent JN, Tucker GE, Coe JA, Kean JW, Smith JB, Staley DM, Kleiber W, Wiens AM (2019) Topographic change detection at Chalk Cliffs, Colorado, USA, using Airborne LiDAR and UAS-based Structure-from-Motion photogrammetry. In: Kean JW, Coe JA, Santi PM, and Guillen BK (eds) Debris-Flow Hazards Mitigation: Mechanics, Monitoring, Modeling, and Assessment, Association of Environmental and Engineering Geologists, Special Publication #28, pp 85-92
- Booth AM, Sifford C, Vascik B, Siebert C, Buma B (2020) Large wood inhibits debris flow runout in forested southeast Alaska. *Earth Surface Processes and Landforms* 45:1555-1568
- Carbonneau PE, Dietrich JT (2017) Cost-effective non-metric photogrammetry from consumer-grade sUAS: implications for direct georeferencing of structure from motion photogrammetry. *Earth Surface Processes and Landforms* 42:473-486
- Chigira M, Ling S, Matsushi Y (2018) Landslide disaster induced by the 2017 northern Kyushu rainstorm. *Disaster Prevention Research Institute Annals, A* 61:28-35 (in Japanese, with English abstract).
- Comiti F, Andreoli A, Lenzi MA, Mao L (2006) Spatial density and characteristics of woody debris in five mountain rivers of the dolomites (Italian Alps). *Geomorphology* 78(1):44-63
- Fonstad MA, Dietrich JT, Courville BC, Jensen JL, Carbonneau PE (2013) Topographic structure from motion: a new development in photogrammetric measurement. *Earth Surface Processes and Landforms* 38(4):755-766
- Gurnell AM, Petts GE, Hannah DM, Smith BPG, Edwards PJ, Kollmann J, Ward JV, Tockner K (2001) Riparian vegetation and island formation along the gravel-bed Riume Tagliamento, Italy. *Earth Surface Processes and Landforms* 26:31-62
- Haga H, Kumagai T, Otsuki K, Ogawa S (2002) Transport and retention of coarse woody debris in mountain streams: an in situ field experiment of log transport and a field survey of coarse woody debris distribution. *Water Resource Research* 38(8):1-1 – 1-16
- Jackson CR, Sturm CA (2002) Woody debris and channel morphology in first and second order forested channels in Washington's coast ranges. *Water Resource Research* 38:1177-1190
- James MR, Robson S (2014) Mitigating systematic error in topographic models derived from UAV and ground-based image networks. *Earth Surface Processes and Landforms* 39:1413-1420
- Johnson AC, Swanston DN, McGee KE (2000) Landslide initiation, runout, and deposition within clearcuts and old-growth forests of Alaska. *Journal of the American Water Resources Association* 36:17-30
- Kaibori M, Hasegawa Y, Yamashita Y, Sakida H, Nakai S, Kuwada S, Hiramatsu S, Jitousono T, Irasawa M, Shimizu O, Imaizumi F, Nakatani K, Kashiwabara Y, Kato N, Torita E, Hirakawa Y, Yoshinaga S, Tanaka K, Hayashi S (2018) Sediment related disaster due to heavy rainfall in Hiroshima prefecture in July, 2018.

Journal of the Japan Society of Erosion Control Engineering 71 (5):43-53 (in Japanese, with English abstract).

Kasprak A, Magilligan FJ, Nislow KH, Snyder NP (2012) A Lidar-derived evaluation of watershed-scale large woody debris sources and recruitment mechanisms: coastal Maine, USA. *River Research and Applications* 28:1462-1476

Keller EA, Swanson FJ (1979) Effects of large organic material on channel form and fluvial processes. *Earth Surface Processes* 4:361-380

Koutsoyiannis D, Kozonis D, Manetas A (1998) A mathematical framework for studying rainfall intensity-duration-frequency relationships. *Journal of Hydrology* 206 (1-2):118-135

Lancaster ST, Hayes SK, Grant GE (2003) Effects of wood on debris flow runout in small mountain watersheds. *Water Resources Research* 39(6):1168

Lisle TE (1995) Effects of coarse woody debris and its removal on a channel affected by the 1980 eruption of Mount St. Helens, Washington. *Water Resources Research* 31:1797-1808

Manners RB, Doyle MW, Small MJ (2007) Structure and hydraulics of natural woody debris jams. *Water Resources Research* 43:W06432

Marutani T, Kaibori M, Jitousono T, Mizuno H, Ohno H, Shimizu O, Kubota T, Ue H, Kanazawa A, Kawano T, Koga S, Kobayashi H, Kobayashi T, Sakashima T, Sakatani Y, Sagara W, Shinohara Y, Suzuki Y, Takagi M, Torita E, Nakano K, Fujisawa Y, Yamaguchi K, Yamada Y (2017) Sediment-related disasters by a heavy rainfall in the northern part of Kyusyu-Island, Japan in July 2017. *Journal of the Japan Society of Erosion Control Engineering* 70(4): 31-42 (in Japanese, with English abstract).

May CL (2002) Debris flows through different forest age classes in the central Oregon Coast Range. *Journal of the American Water Resources Association* 38(4):1097-1113

May CL, Gresswell RE (2003a) Large wood recruitment and redistribution in headwater streams in the Southern Oregon Coast Range, USA. *Canadian Journal of Forest Research* 33:1352-1362

May CL, Gresswell RE (2003b) Processes and rates of sediment and wood accumulation in headwater streams of the Oregon Coast Range, USA. *Earth Surface Processes and Landforms* 28:409-424

Montgomery DR, Buffington JM, Smith R, Schmidt K, Pess G (1995) Pool spacing in forest channels. *Water Resources Research* 31:1097-1105

Montgomery DR, Abbe TB, Peterson NP, Buffington JM, Schmidt K, Stock JD (1996) Distribution of bedrock and alluvial channels in forested mountain drainage basins. *Nature* 381:587-589

- Nakamura F, Swanson FJ (1993) Effects of coarse woody debris on morphology and sediment storage of a mountain stream system in western Oregon. *Earth Surface Processes and Landforms* 18:43-61
- Nakamura F, Seo J-II, Akasaka T, Swanson FJ (2017) Large wood, sediment, and flow regimes: Their interactions and temporal changes caused by human impacts in Japan. *Geomorphology* 279:176–187
- Piton G, Recking A (2016) Design of sediment traps with open check dams. II: woody debris
Journal of Hydraulic Engineering 142(2):1-17
- Ravazzolo D, Mao L, Picco L, Lenzi MA (2015) Tracking log displacement during floods in the Tagliamento River using RFID and GPS tracker devices. *Geomorphology* 228:226-233
- Ruiz-Villanueva V, Bodoque JM, Díez-Herrero A, Eguibar MA, Pardo-Igúzquiza E (2013) Reconstruction of a flash flood with large wood transport and its influence on hazard patterns in an ungauged mountain basin. *Hydrological Processes* 27(24):3424-3437
- Ruiz-Villanueva V, Piégay H, Gurnell AM, Marston RA, Stoffel M (2016) Recent advances quantifying the large wood dynamics in river basins: New methods and remaining challenges. *Reviews of Geophysics* 54(3):611-652
- Sane Y, Panthou G, Bodian A, Vischel T, Lebel T, Dacosta H, Quantin G, Wilcox C, Ndiaye O, Diongue-Niang A, Kane MD (2018) Intensity–duration–frequency (IDF) rainfall curves in Senegal. *Natural Hazards and Earth System Sciences* 18:1849-1866
- Sanhueza D, Picco L, Ruiz-Villanueva V, Iroumé A, Ulloa H, Barrientos G (2019) Quantification of fluvial wood using UAVs and structure from motion. *Geomorphology* 345:106837
- Swanson FJ, Gregory SV, Iroumé A, Ruiz-Villanueva V, Wohl E (2020) Reflection on the history of research on large wood in rivers. *Earth Surface Processes and Landforms* (in press)
- Tang YJ, Xu ZM, Yang TQ, Zhou ZH, Wang K, Ren Z, Yang K, Tian L (2018) Impacts of small woody debris on slurring, persistence, and propagation in a low-gradient channel of the Dongyuege debris flow in Nu River, Southwest China. *Landslides* 15:2279-2293
- Tsuguti H, Seino N, Kawase H, Imada Y, Nakaegawa T, Takayabu I (2019) Meteorological overview and mesoscale characteristics of the Heavy Rain Event of July 2018 in Japan. *Landslides* 16:363-371.
- Tsunetaka H, Hotta N, Hayakawa YS, Imaizumi F (2020) Spatial accuracy assessment of unmanned aerial vehicle-based structures from motion multi-view stereo photogrammetry for geomorphic observations in initiation zones of debris flows, Ohya landslide, Japan. *Progress in Earth and Planetary Science* 7(24): doi 10.1186/s40645-020-00336-0

Ulloa H, Iroumé A, Mao L, Andreoli A, Diez S, Lara LE (2015) Use of remote imagery to analyse changes in morphology and longitudinal large wood distribution in the Blanco River after the 2008 Chaitén volcanic eruption, southern Chile. *Geografiska Annaler: Series A, Physical Geography* 97:523-541

Wallace JB, Benke AC (1984) Quantification of wood habitat in subtropical coastal plain streams. *Canadian Journal of Fisheries and Aquatic Science* 41:1643-1652

Woodsmith RD, Buffington JM (1996) Multivariate geomorphic analysis of forest streams: implications for assessment of land use impact on channel condition. *Earth Surface Processes and Landforms* 21:377-393

Wyżga B, Mikuś, P., Zawiejska, J., Ruiz-villanueva, V., Kaczka, R. J., & Czech, W (2017) Log transport and deposition in incised, channelized, and multithread reaches of a wide mountain river: Tracking experiment during a 20-year flood. *Geomorphology* 279:98-111

Tables

Table 1. Properties of the UAV and the installed camera.

UAV	
Model	DJI Mavic 2 pro
Weight	907 g
Diagonal size	354 mm
Max. duration of flight	31 min
Camera	
Number of pixels	20 M
Sensor size	13.2 × 8.8 mm
Focal length	∞

Table 2. Dates of UAV flights and number of aerial images used to provide ortho-photographs.

	Date	Number of aerial images
CF site		
First flight	February 14, 2019	159
Second flight	September 26, 2019	284
BF site		
First flight	November 16, 2018	315
Second flight	December 25, 2019	141

Table 3. Return period (RP) for the annual maxima of rainfall intensities at the CF site.

	RP_{1h}	RP_{2h}	RP_{3h}	RP_{6h}	RP_{12h}	RP_{24h}	RP_{48h}	RP_{72h}
	(year)							
2017	> 100	> 100	> 100	> 100	> 100	> 100	> 100	> 100
2018	1.66	2.68	3.47	10.84	17.60	20.70	33.67	17.05
2019	10.32	11.98	14.18	33.46	32.22	15.86	11.17	11.31

Table 4. Return period (RP) for the annual maxima of rainfall intensities at the BF site.

	RP_{1h}	RP_{2h}	RP_{3h}	RP_{6h}	RP_{12h}	RP_{24h}	RP_{48h}	RP_{72h}
	(year)							
2018	15.60	14.67	11.88	13.70	> 100	> 100	> 100	> 100
2019	3.77	2.76	1.90	2.36	2.13	2.00	1.77	1.67

Figures

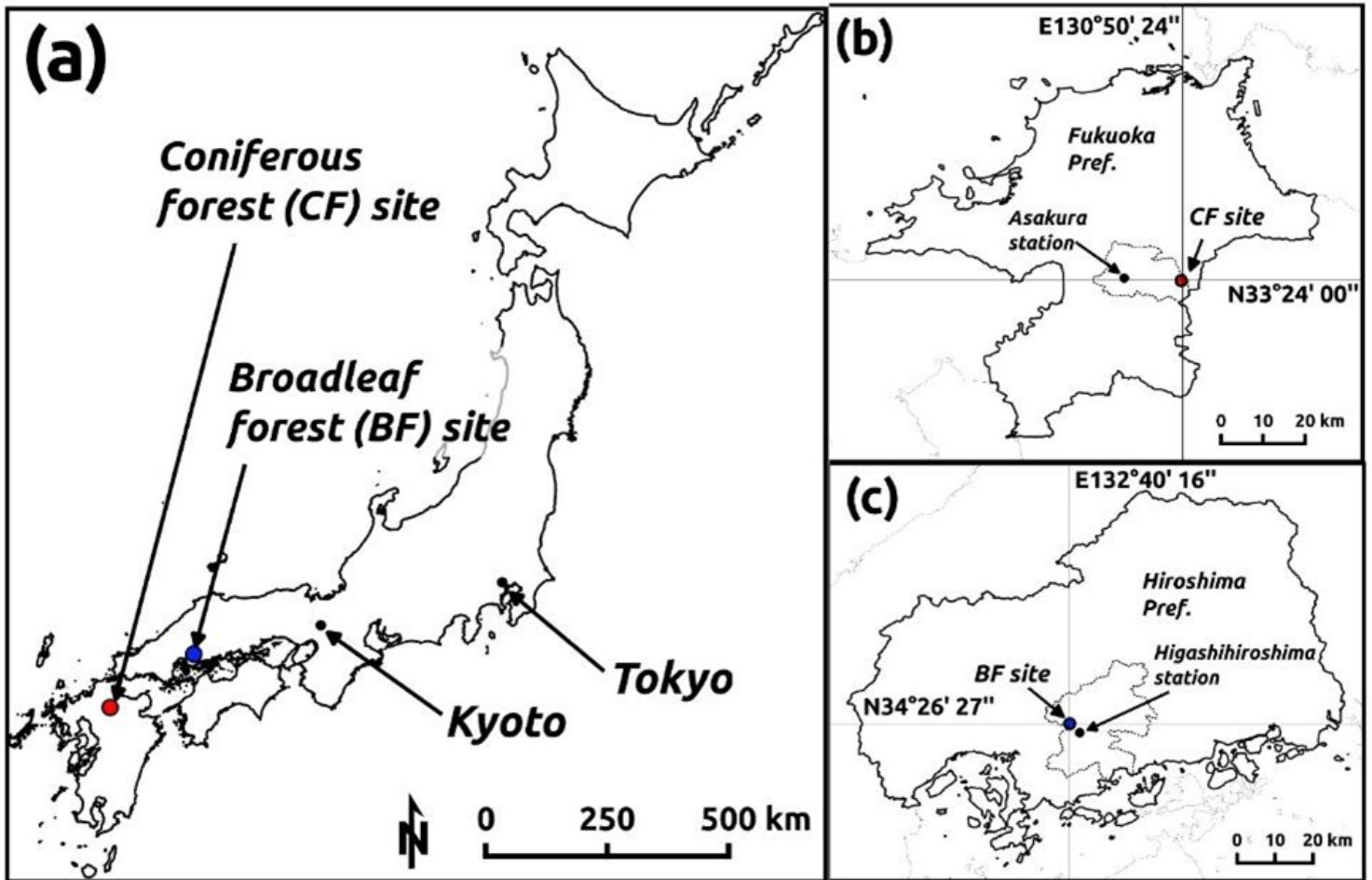


Figure 1

Study site: (a) overview, (b) locations of the coniferous forest (CF) site and the rain-gauge station (Asakura station), and (c) locations of the broadleaf forest (BF) site and the rain-gauge station (Higashihiroshima station).

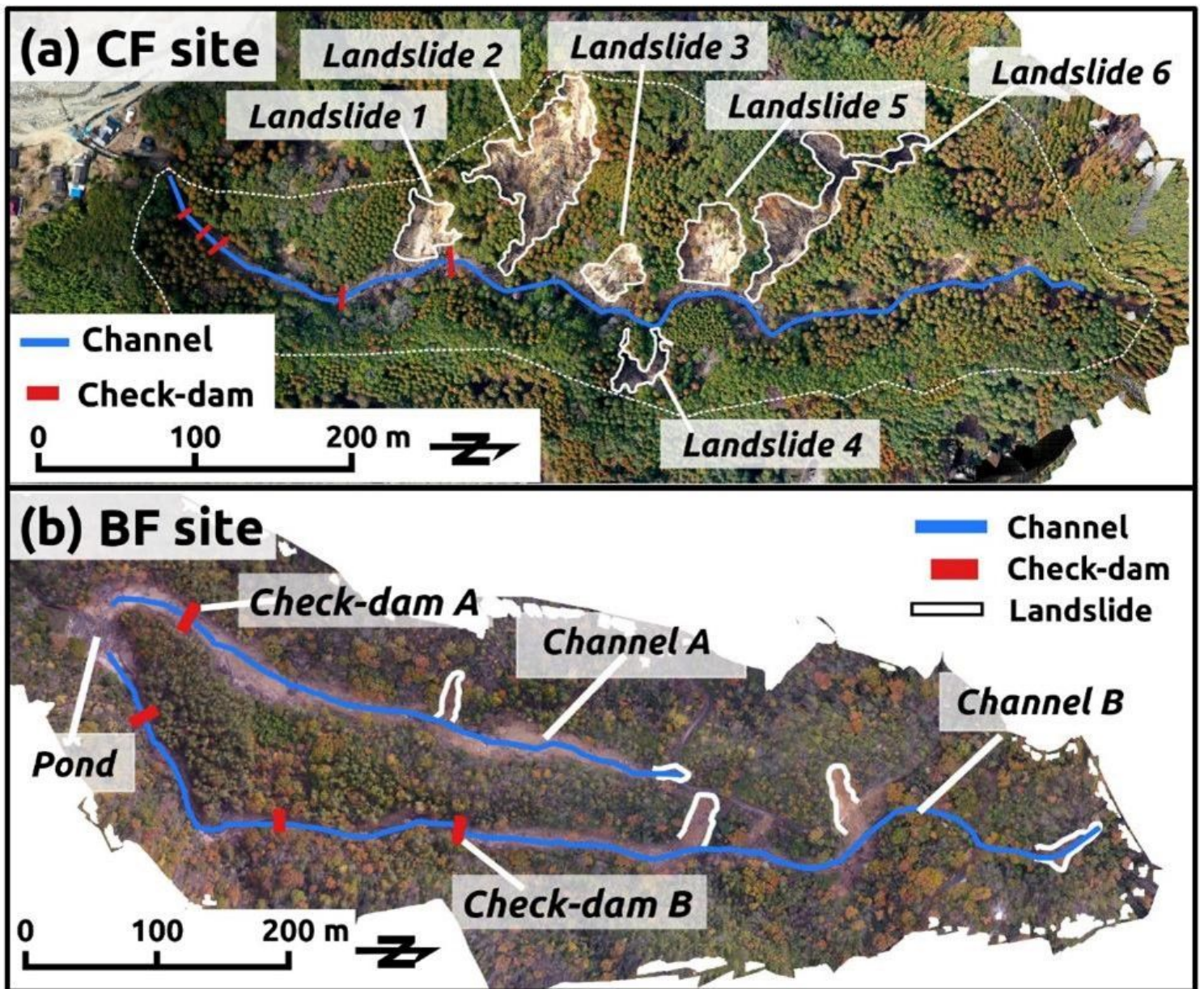
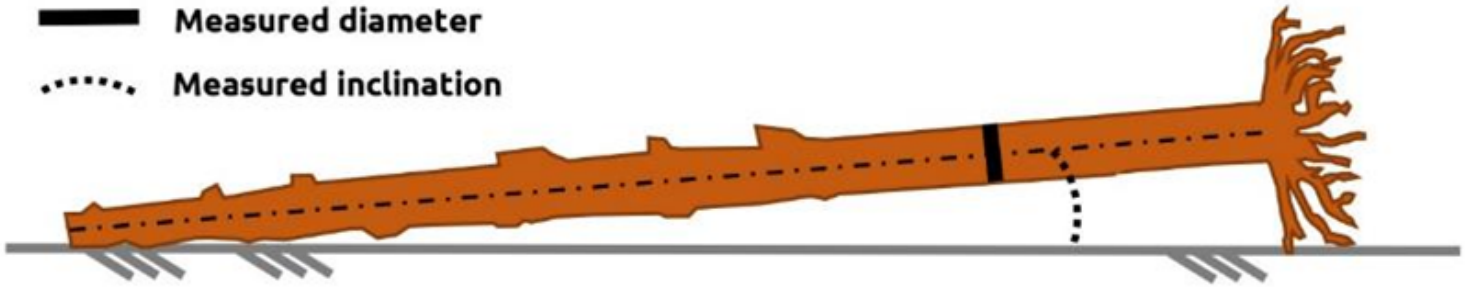


Figure 2

Ortho-photograph of the study sites: (a) the coniferous forest (CF) site and (b) the broadleaf forest (BF) site. The right side indicates the upper part of the channel (i.e., the streams descend from north to south).

(a) Coniferous tree

- - - - - Measured length
- █ Measured diameter
- ⋯ Measured inclination



(b) Broadleaf tree

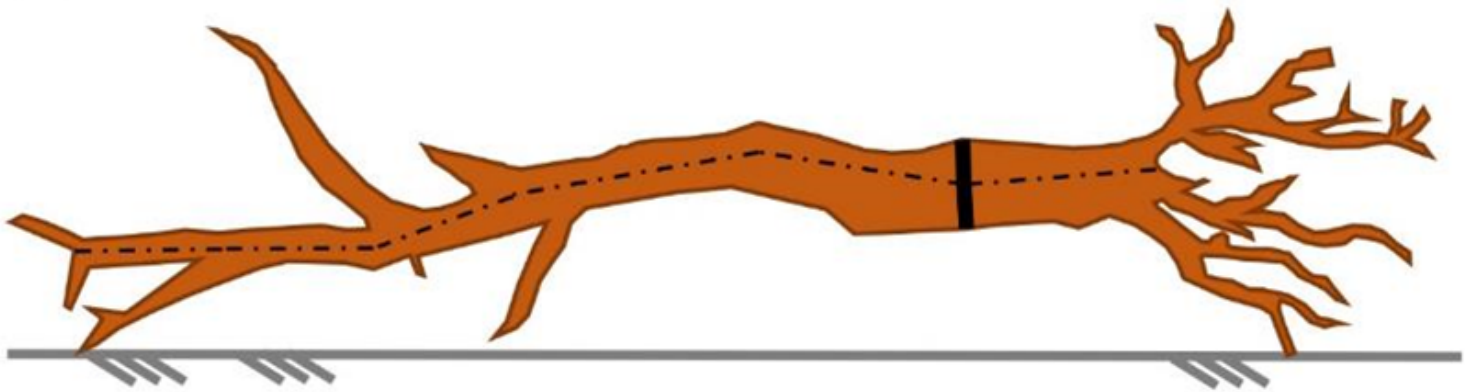


Figure 3

Schematic representation of the components for the direct measurement of large wood (LW): (a) the coniferous tree and (b) broadleaf tree. The left side indicates the top of each type of tree (the side of the tree crown). The right side depicts the root-wad.

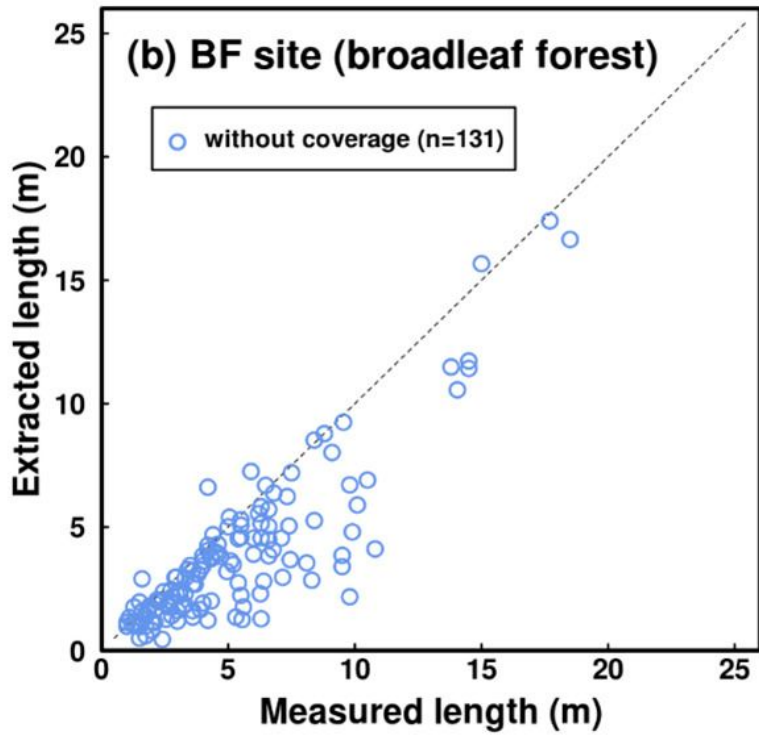
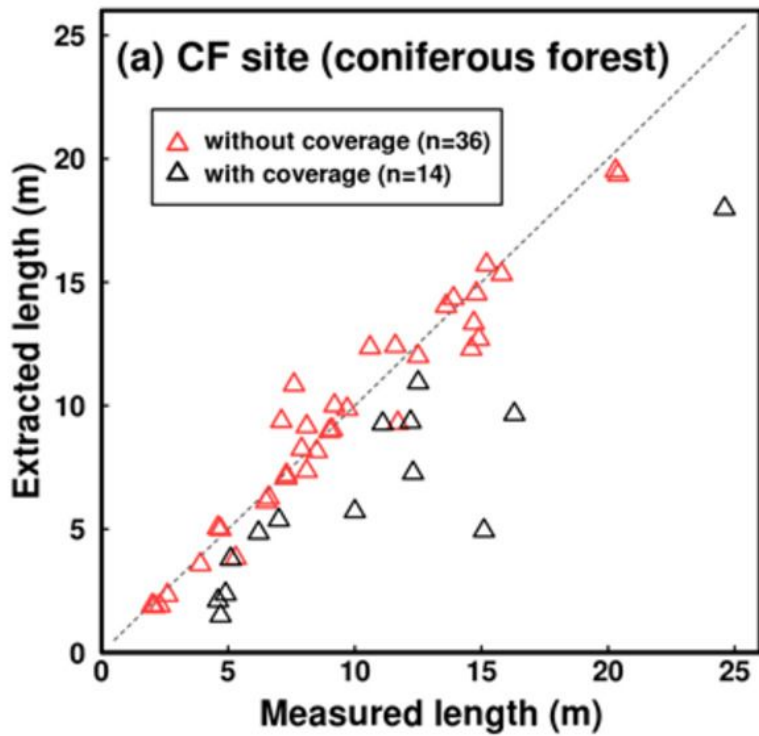


Figure 4

Comparison between extracted and measured lengths of large wood (LW): (a) the coniferous forest (CF) site and (b) the broadleaf forest (BF) site.

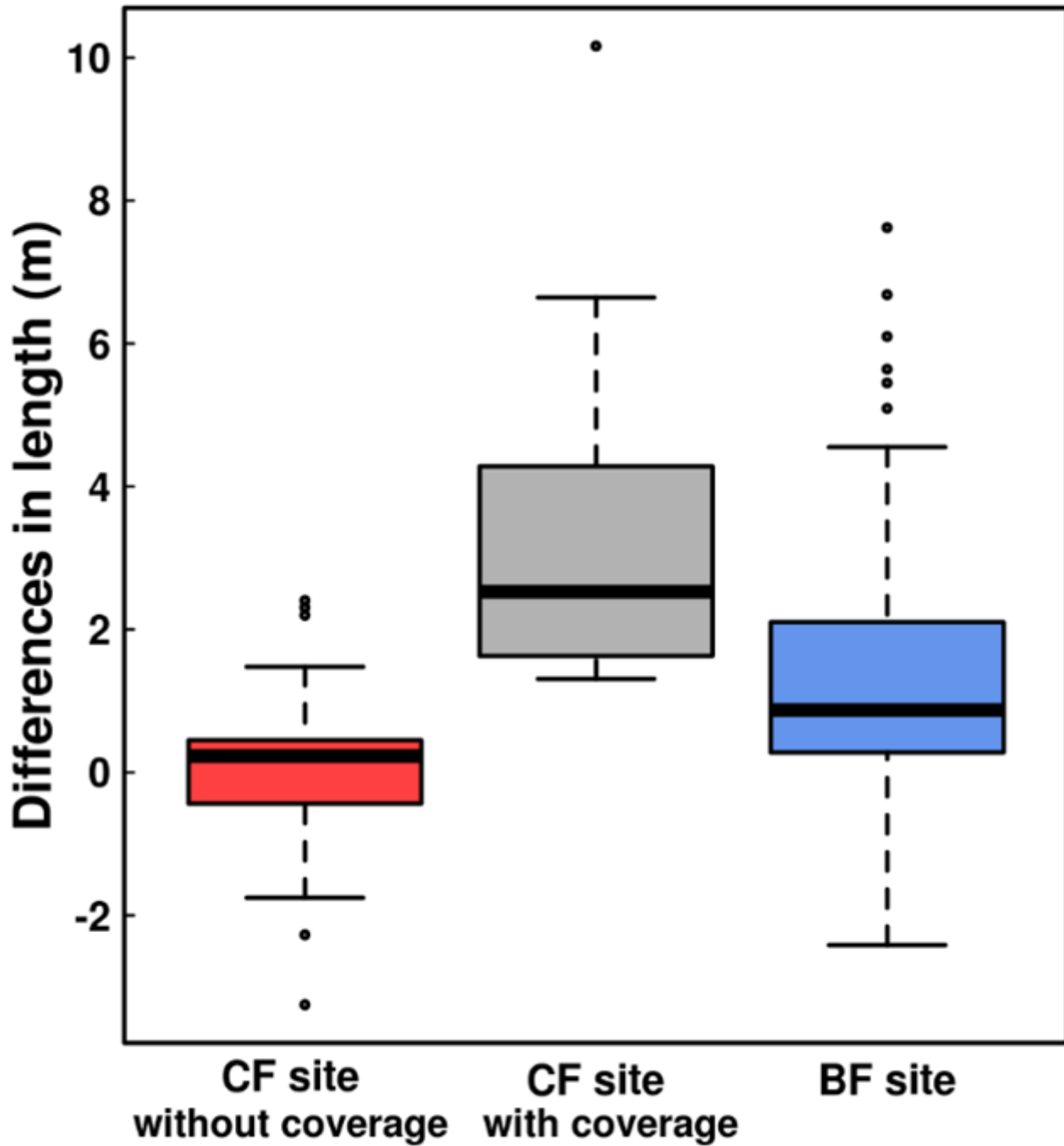


Figure 5

Boxplot of differences between the extracted and measured lengths of the large wood (LW). Differences in length were calculated by subtracting the extracted length from the measured length.

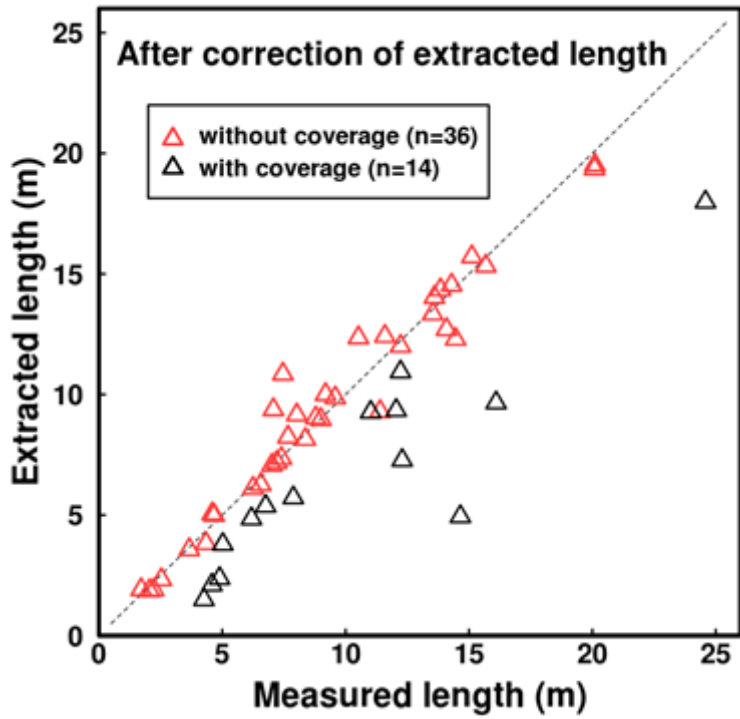


Figure 6

Comparison between corrected extracted length and measured length of the large wood (LW) at the coniferous forest (CF) site. The corrected extracted length indicates that the inclined length was corrected from the extracted length (i.e., orthogonally projected length) using the directly measured inclination of the LW.

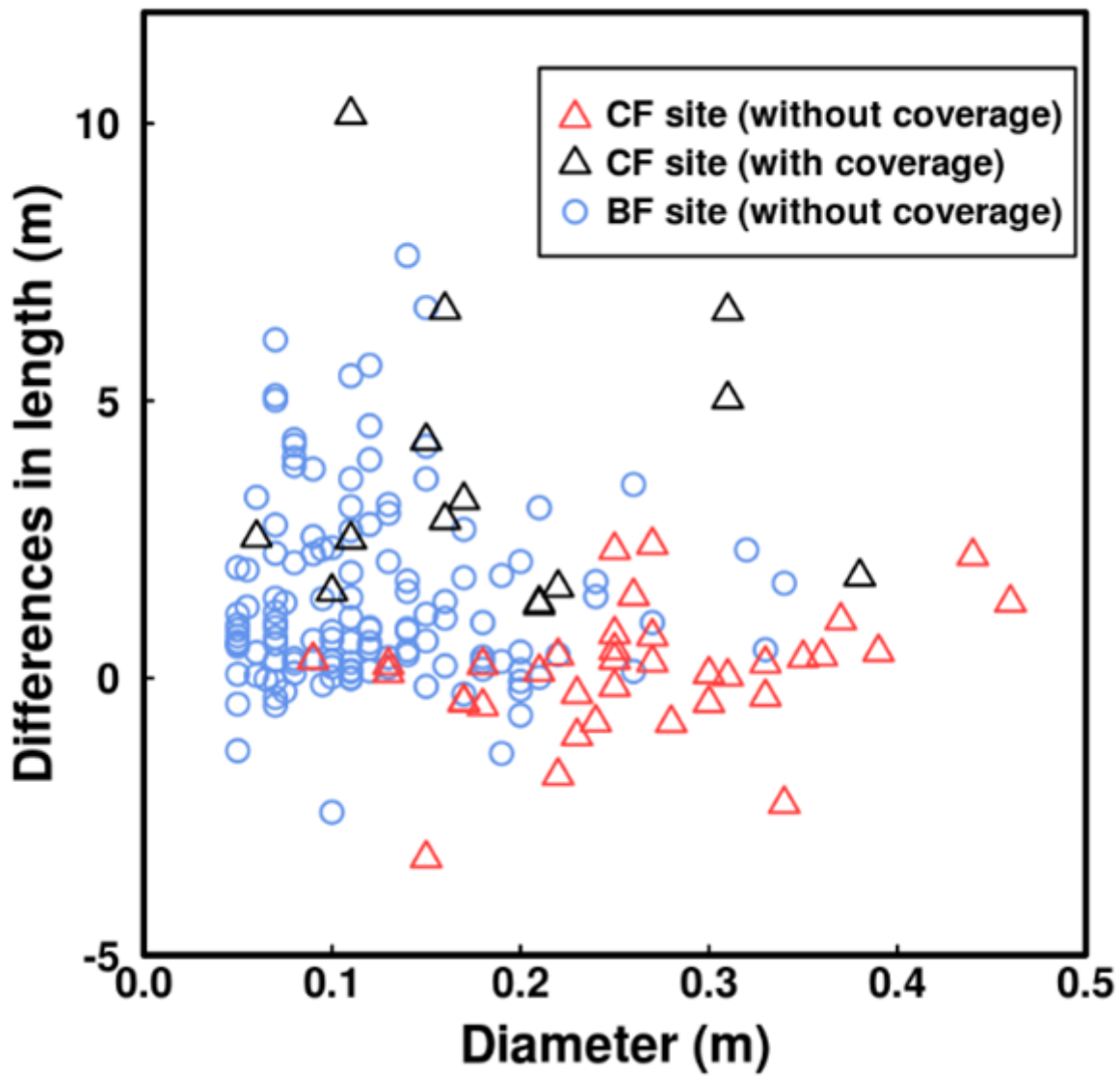


Figure 7

The differences between the extracted and measured lengths of the large wood (LW) as functions of the measured diameter. Differences in length were calculated by subtracting the extracted length from the measured length, similar to Figure 5.

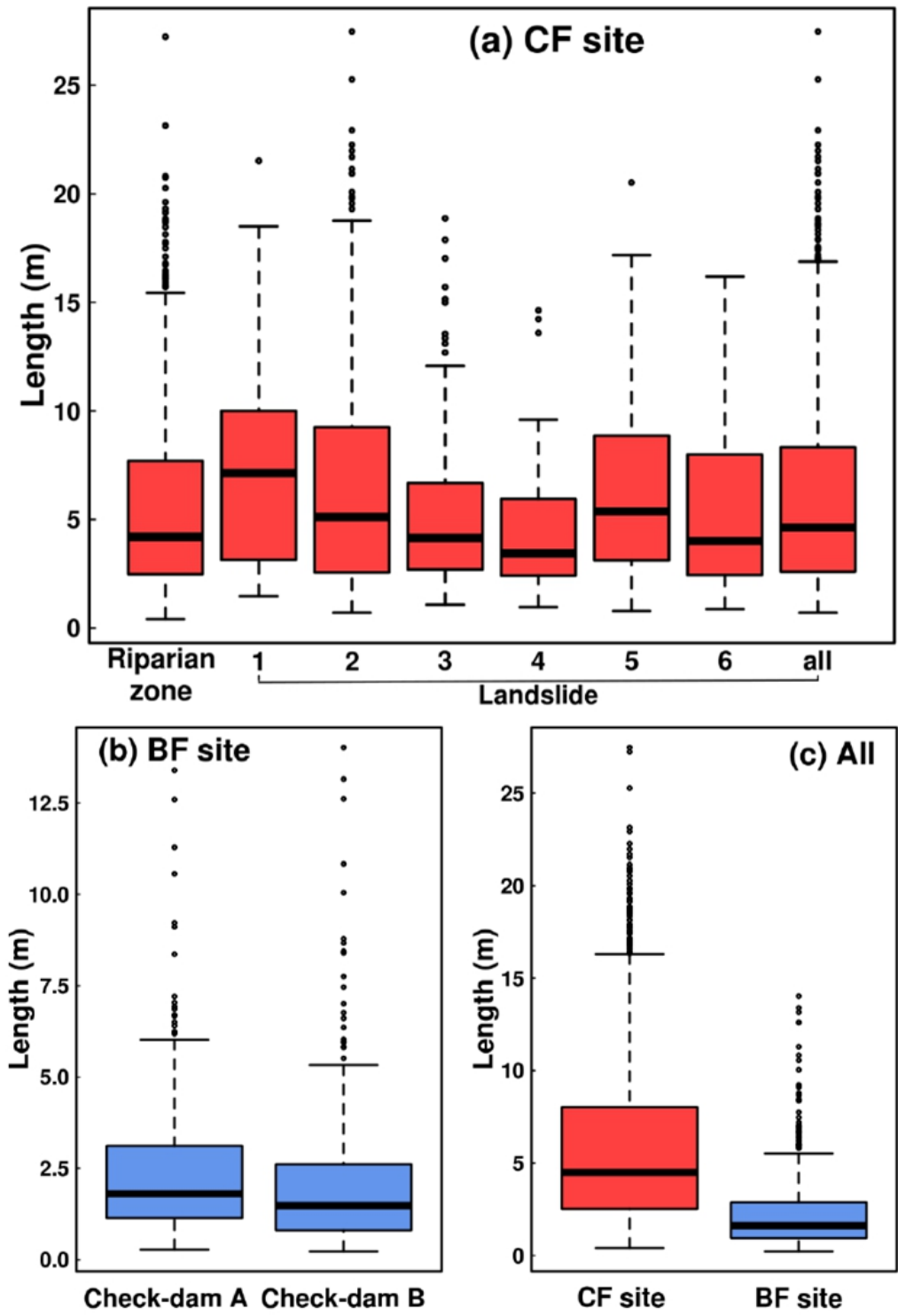


Figure 8

Boxplots of the extracted lengths: (a) the coniferous forest (CF) site, (b) the broadleaf forest (BF) site, and (c) all measured lengths. In panel (a), the labels of the landslides correspond to Figure 2a (“All” indicates the total number of landslides). The large wood (LW) extracted in the area excluding landslide scars was regarded as the riparian zone (Figure 10).

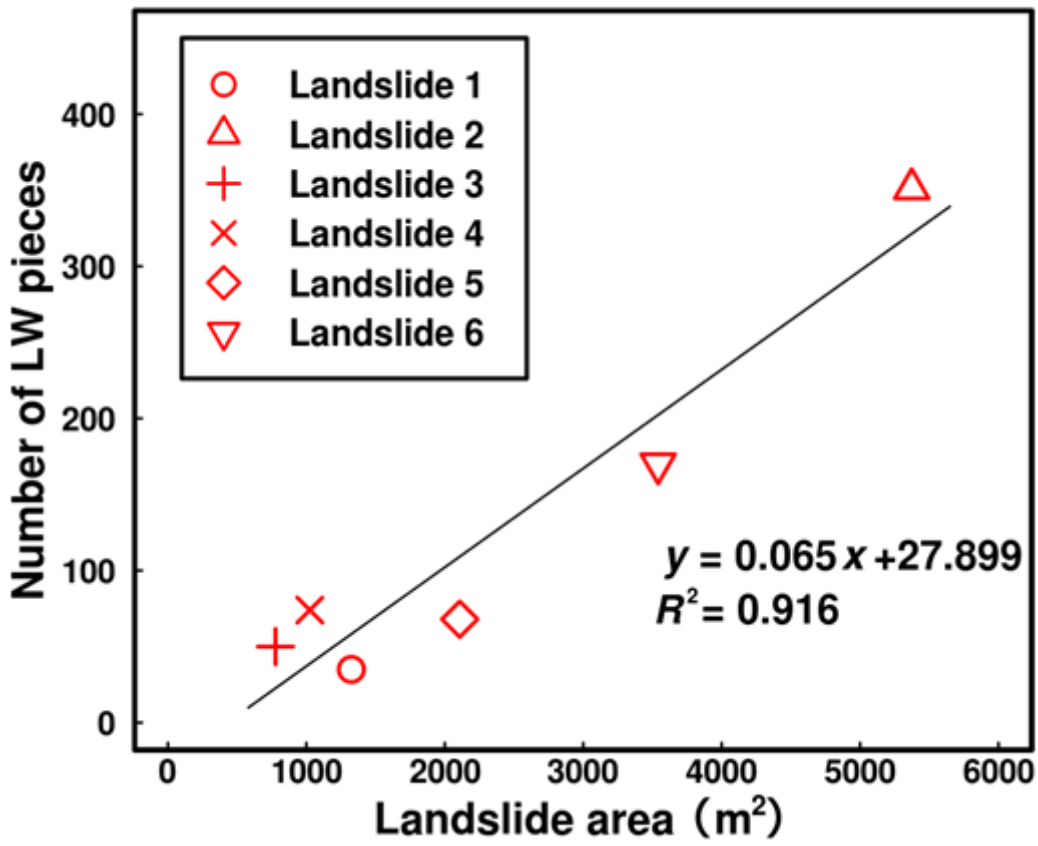


Figure 9

Comparison between landslide area and number of remaining large wood (LW) pieces. The black line is the linear regression line.

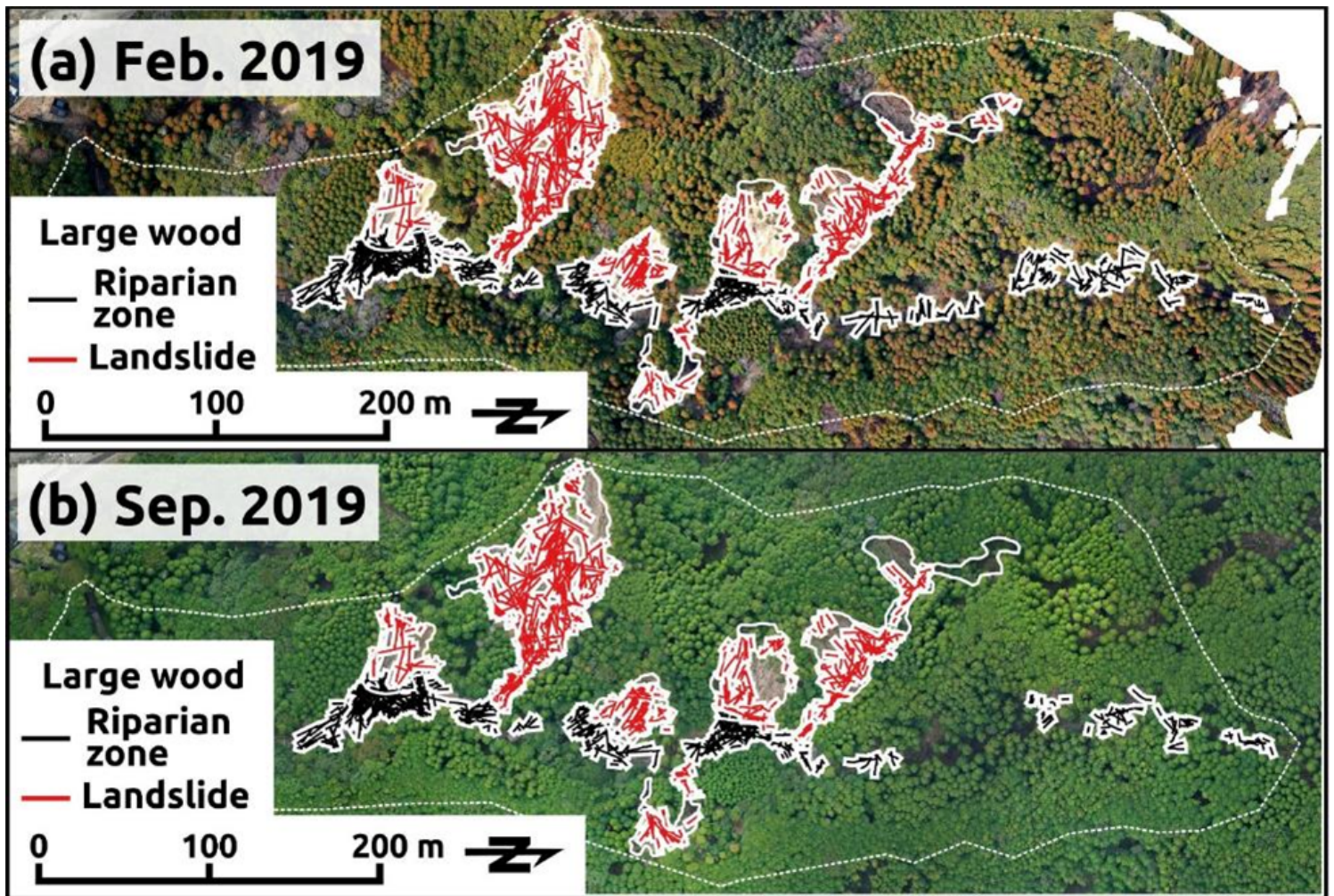


Figure 10

Spatial distribution of extracted large wood (LW) at the coniferous forest (CF) site: (a) February 14, 2019, and (b) September 26, 2019.

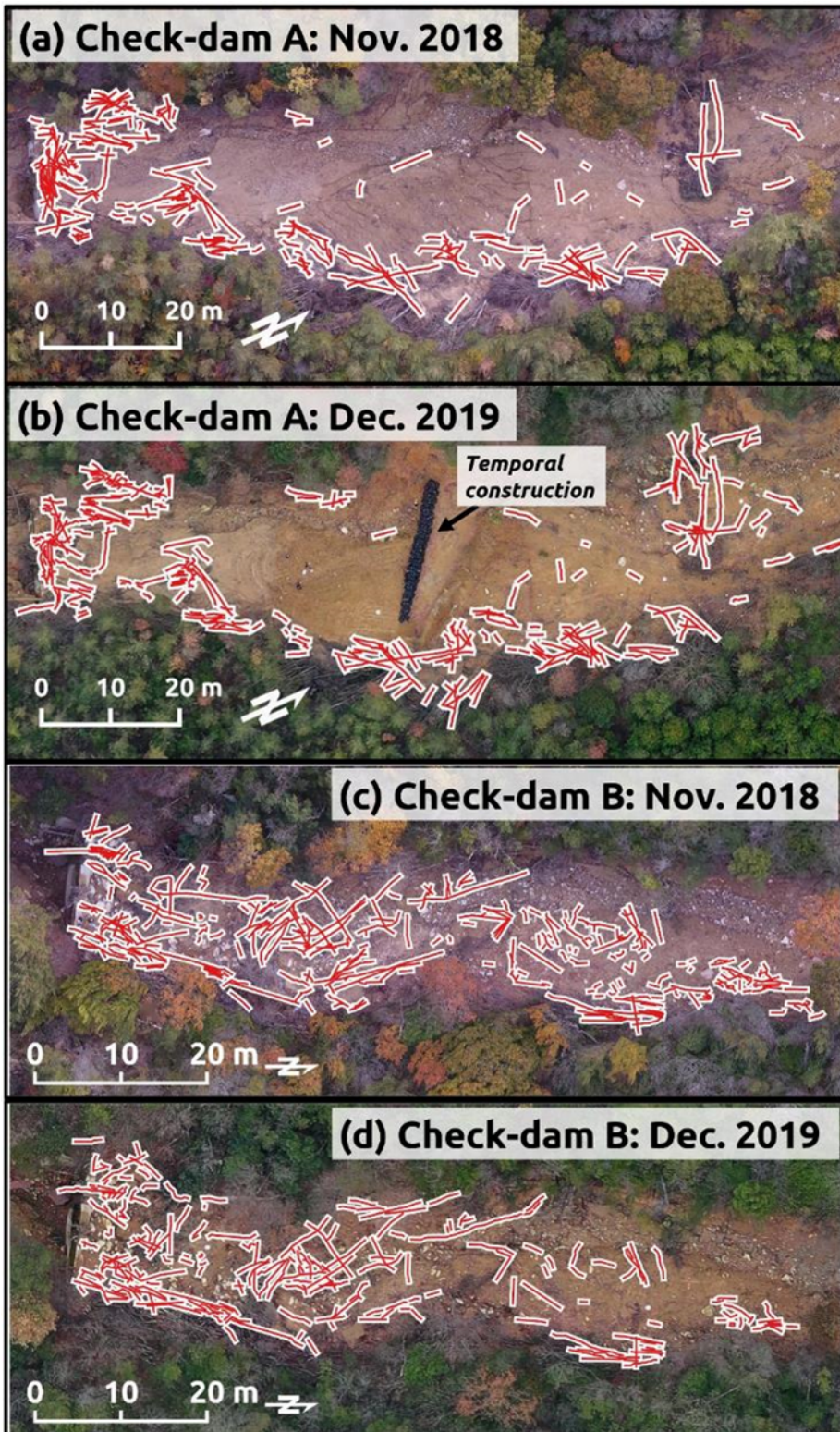


Figure 11

Spatial distribution of extracted large wood (LW) at the broadleaf forest (BF) site: (a) check-dam A on November 16, 2018, (b) check-dam A on December 25, 2019, (c) check-dam B on November 16, 2018, and (d) check-dam B on December 25, 2019.

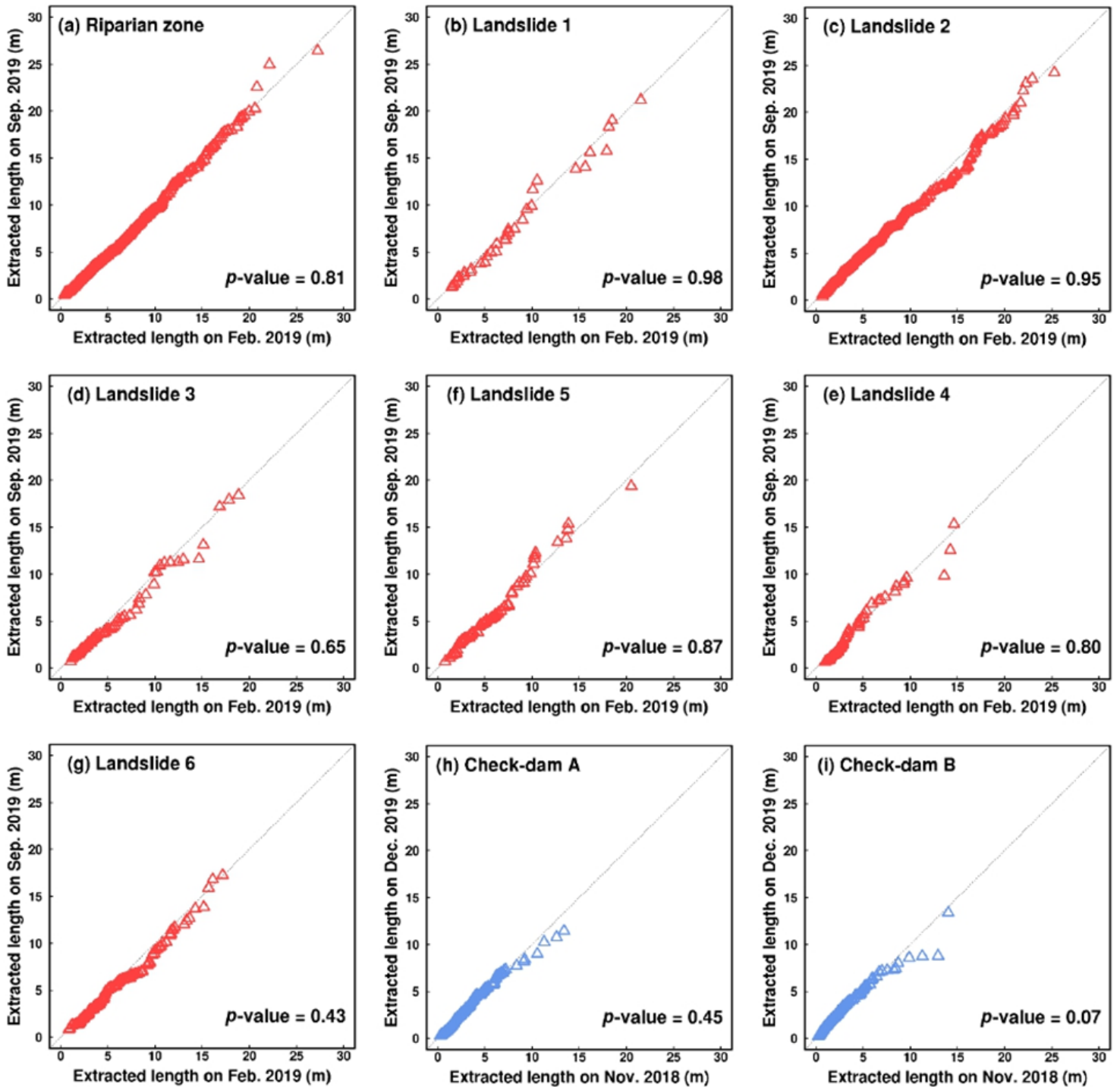


Figure 12

Q–Q plots for the lengths of the extracted large wood (LW): (a–g) the coniferous forest (CF) site and (h–i) the broadleaf forest (BF) site. The p -value indicates the result of the goodness-of-fit test (the Kolmogorov–Smirnov test).

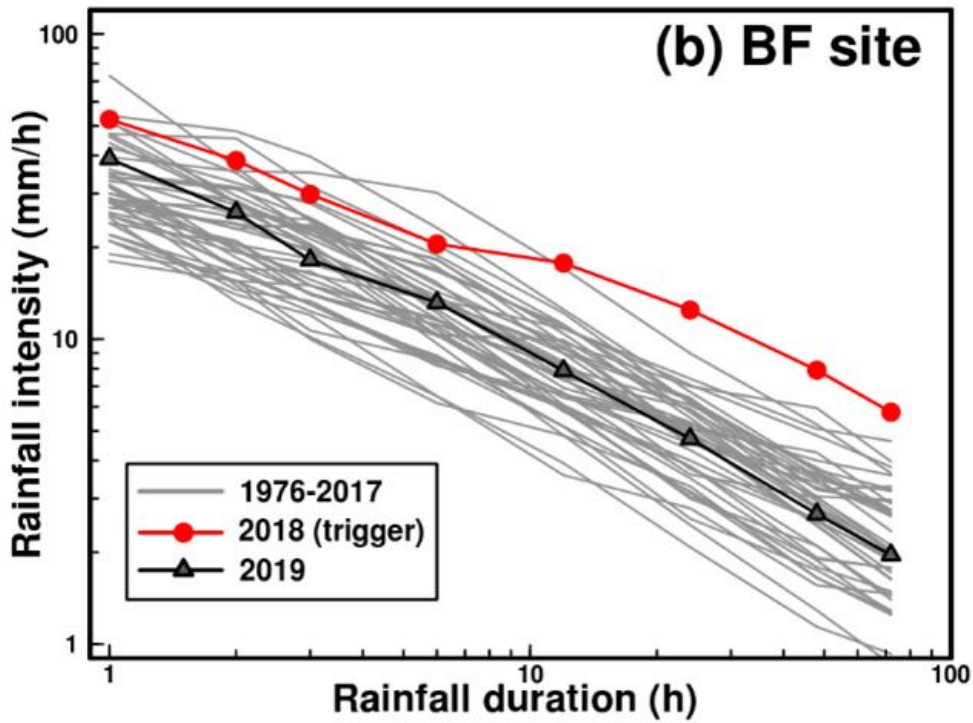
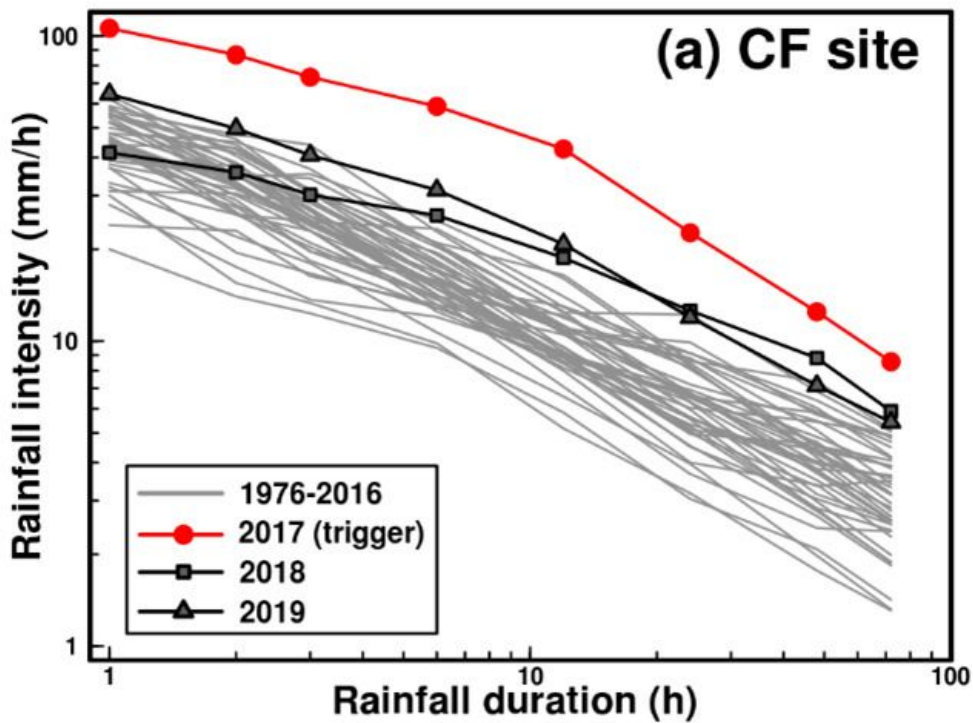


Figure 13

Curves for the annual maxima of rainfall intensity: (a) the coniferous forest (CF) site and (b) the broadleaf forest (BF) site.

Supplementary Files

This is a list of supplementary files associated with this preprint. Click to download.

- [GraphicalAbstract.jpg](#)